Supporting Information

$Bi_3O_{2.5}Se_2$: A Two-Dimensional High-Mobility Polar Semiconductor with Large Interlayer and Interfacial Charge Transfer

Xinyue Dong[1], Yameng Hou[1], Chaoyue Deng[2], Jinxiong Wu[1], Huixia Fu[2,3*]*

[1]Tianjin Key Lab for Rare Earth Materials and Applications, Center for Rare Earth and Inorganic Functional Materials, Smart Sensor Interdisciplinary Science Center, School of Materials Science and Engineering, Nankai University, Tianjin 300350, P. R. China

[2]Center of Quantum Materials and Devices, College of Physics, Chongqing University, Chongqing 401331, P. R. China

[3]Chongqing Key Laboratory for Strongly Coupled Physics, Chongqing University, Chongqing 401331, P. R. China

[*]Corresponding author. Email: hxfu@cqu.edu.cn; jxwu@nankai.edu.cn

Supplementary Figures and Tables

Part I: Ab-initio molecular dynamics (AIMD) simulations in monolayer $Bi_3O_{2.5}Se_2$

To verify thermodynamic stability, we performed ab-initio molecular dynamics (AIMD) simulations in monolayer $Bi_3O_{2.5}Se_2$. We constructured a 3x3 supercell with lattice parameters a=21.56 Å, b=12.30 Å, containing 135 atoms. The geometric

structure of the top and side views after AIMD simulation at 300 K are shown in Figure S1a, indicating that the structure remains intact. Additionally, the energy fluctuations over time, shown in Figure S1b, are minimal, confirming the thermodynamic stability of the monolayer $Bi_3O_{2.5}Se_2$ at room temperature.

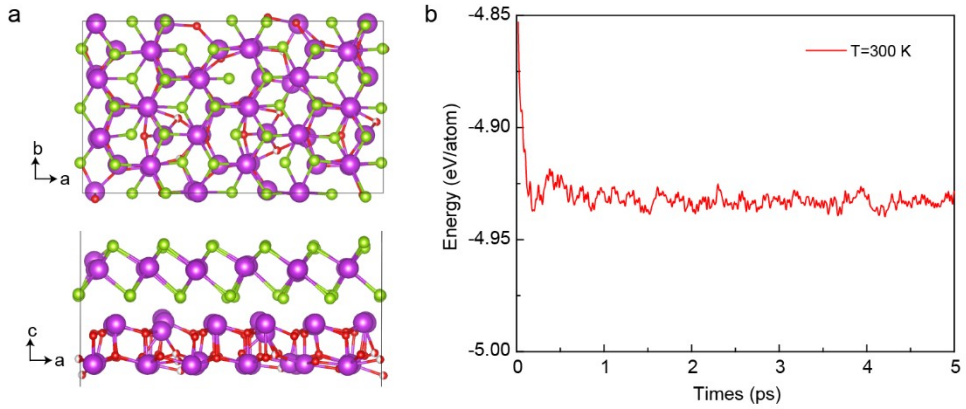

Figure S1. (a) The geometric structures of top and side views of a monolayer $Bi_3O_{2.5}Se_2$ after the ab-initio molecular dynamics simulation at 300 K. (b) The corresponding energy fluctuations concerning time in AIMD simulations.

Furthermore, $Bi_3O_{2.5}Se_2$ nanoplates have been grown experimentally, as seen in Figure S2a, which shows a flat surface with a height of 1.1 nm (Figure S2b). The micro-topography was monitored after exposure to air by atomic force microscopy (AFM), as shown in Figure S2c-d. Remarkably, the sample undergoes undetectable surface roughness changes, even after air exposure for ten days, indicating excellent air stability. Moreover, in our article (Laser. Photonics. Rev., 2024, 18, 2300854), we also demonstrated that the samples of thin films with few-layers thickness maintain excellent air stability.

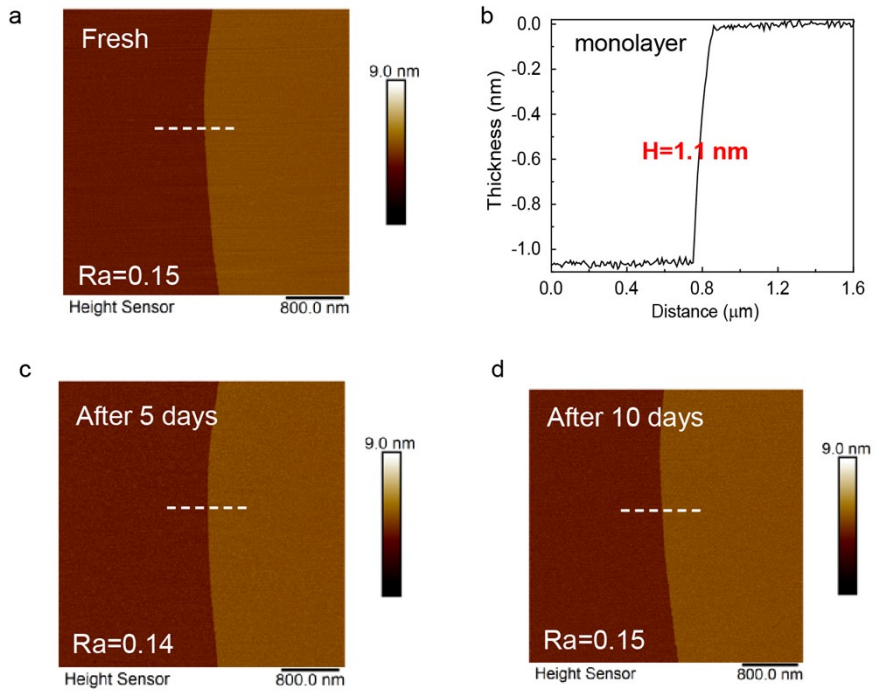

Figure S2. (a) AFM image of a fresh monolayer $Bi_3O_{2.5}Se_2$ nanoplate. (b) The result of thickness measurement of monolayer. (c-d) The sample exposed to air for different days, showing constant roughness values.

Part II: Transport properties calculated based on semi-empirical Boltzmann transport theory

We have also employed a semi-empirical Boltzmann transport approach, similar to the one used in the references Phys. Chem. Chem. Phys., 2015, 17, 6865-6873, and Phys. Chem. Chem. Phys., 2016, 18, 16345-16352, to calculate transport properties at room temperature using the constant relaxation time approximation.

We calculated the conductivity(σ) /relaxation time (τ) as shown in Figure S3a using VASPKIT software (Comput. Phys. Commun. 267, 108033 (2021)). The relaxation time τ can be obtained from the method of deformation potential (DP) theory with the value of 285 fs. The mobility μ at 300K, derived using the Boltzmann

transport theory, is approximately 716 $cm^2 V^{-1} s^{-1}$, which remains relatively high.

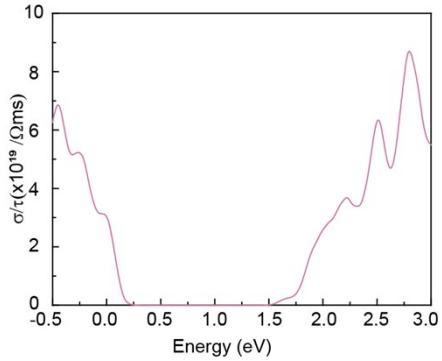

Figure S3. Transport properties calculated based on semi-empirical Boltzmann transport theory using VASPKIT software. Conductivity(σ)/relaxation time (τ) as a function of Fermi level.

Part III: Comparison of electrostatic potential with/without dipole correction in monolayer $Bi_3O_{2.5}Se_2$

In our study, we incorporated the dipole correction provided by VASP to account for the asymmetry in the electrostatic potential due to the inherent dipole moment in the system. The dipole correction method (Phys. Rev. B., 1999, 59, 12301) helps to correct the electrostatic potential across periodic boundaries, ensuring accurate calculations. The electrostatic potential of the monolayer $Bi_3O_{2.5}Se_2$ with dipole correction is shown in Figure S4a, while the electrostatic potential without dipole correction is shown in Figure S4b. This comparison clearly illustrates the effect and importance of incorporating the dipole correction in our study.

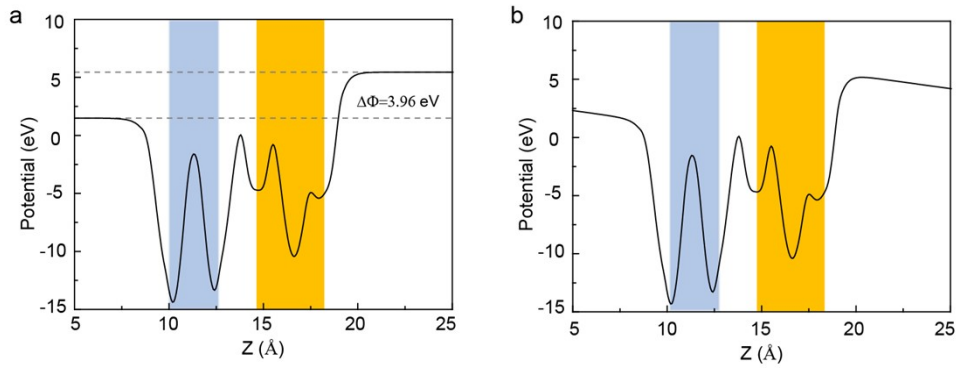

Figure S4. Comparison of electrostatic potential with dipole correction (a) and without dipole correction (b).

Part IV: Lattice mismatch analysis

For the $Bi_3O_{2.5}Se_2$ monolayer, the lattice constants are determined to be a_1=7.19 Å and b_1=4.10 Å. The optimized freestanding graphene monolayer exhibits lattice constants of a_2=7.40 Å and b_2=4.28 Å. Utilizing the formula $\eta = \frac{2(|a_1 - a_2|)}{a_1 + a_2}$ for lattice mismatch calculation, we quantified the lattice mismatch between these two materials. The results indicate a lattice mismatch of 2.9% in the *x* direction and 4.3% in the *y* direction. Notably, both values fall within the acceptable 5% threshold, suggesting high compatibility and potential for effective heterojunction formation between $Bi_3O_{2.5}Se_2$ and graphene.

Part V: Work function of $Bi_3O_{2.5}Se_2$ and graphene

The unique structural composition of the $Bi_3O_{2.5}Se_2$ monolayer, characterized by its inherent polarity features, manifests in distinctive work functions at its upper and lower interfaces. The calculated work function (W_F) at the $[Bi_2O_{2.5}]^+$ terminal registers at 1.99 eV, while the $[BiSe_2]^-$ terminal exhibits a significantly higher W_F of 5.95 eV, as depicted in Figure S5a. In contrast, the graphene monolayer possesses a more

moderate W_F of 4.26 eV in Figure S5b. This intermediary value intriguingly positions graphene between the two polarized terminals of $Bi_3O_{2.5}Se_2$, suggesting diverse charge transfer dynamics upon interaction. Specifically, it implies that graphene may experience contrasting charge transfer directions when interfacing with the $[Bi_2O_{2.5}]^+$ and $[BiSe_2]^-$ terminals. This phenomenon underscores the potential for intricate electronic interplay within the $Bi_3O_{2.5}Se_2$/graphene heterostructure. Besides, when recalculating the WF using the average lattice constants of these two, we obtained similar results as presented above in Figure S5c and Figure S5d.

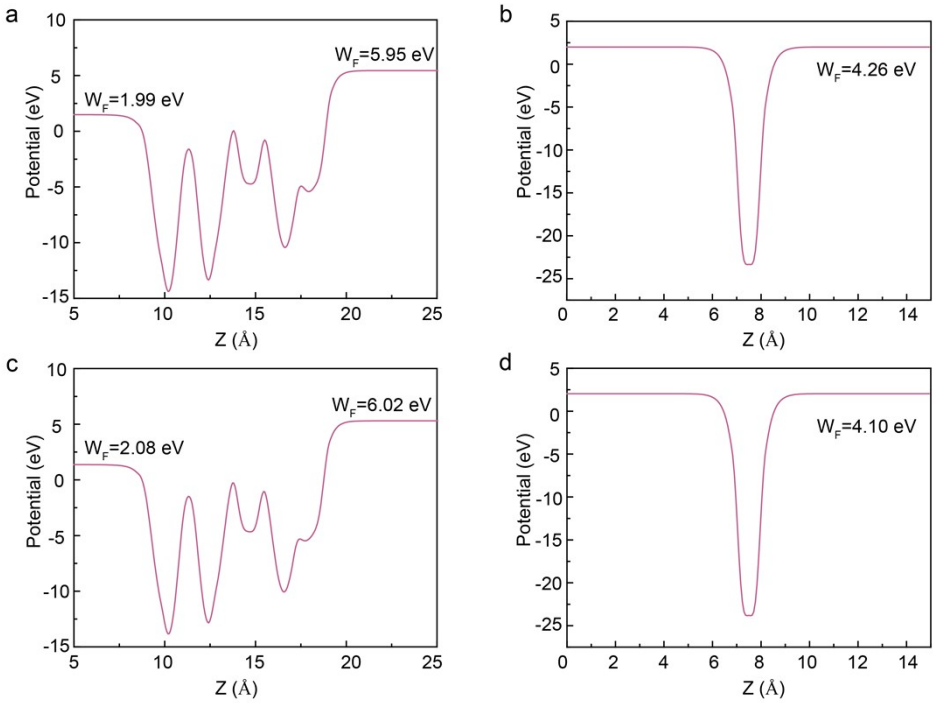

Figure S5. (a) Electrostatic potential of the $Bi_3O_{2.5}Se_2$ monolayer, showcasing the intrinsic polarity and differential work functions (WFs) at each interface. (b) Electrostatic potential of the graphene monolayer with a moderate WF. (c) and (d), Electrostatic potential of the $Bi_3O_{2.5}Se_2$ monolayer and graphene monolayer with the similar outcome as above when utilizing the average lattice constants of these two.

Part VI: Band structure modulation of graphene by varying VCA parameters

The band structure of graphene undergoes notable changes with adjustments in the VCA parameters, particularly affecting the position of the Dirac cone relative to the Fermi level (E_f). As depicted in Figure S6, reducing the VCA parameter results in a downward shift of E_f, while an increase in the parameter causes E_f to move upward. The VCA method simulation of electric fields achieves distinct doping types in graphene.

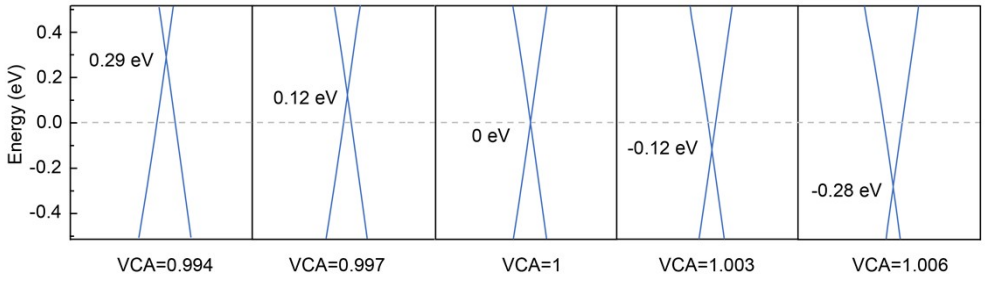

Figure S6. The position of the Dirac cone relative to the Fermi level varies with the VCA parameters. A gray dashed line indicates the Fermi level.